

Unlocking the Power of Boltzmann Machines by Parallelizable Sampler and Efficient Temperature Estimation

Kentaro Kubo^{1,*} and Hayato Goto^{1,2}

¹Corporate Laboratory, Toshiba Corporation, Kawasaki, Kanagawa 212-8582, Japan

²RIKEN Center for Quantum Computing (RQC), Wako, Saitama 351-0198, Japan

(Dated: December 3, 2025)

Boltzmann machines (BMs) are powerful energy-based generative models, but their heavy training cost has largely confined practical use to Restricted BMs (RBMs) trained with an efficient learning method called contrastive divergence. More accurate learning typically requires Markov chain Monte Carlo (MCMC) Boltzmann sampling, but it is time-consuming due to the difficulty of parallelization for more expressive models. To address this limitation, we first propose a new Boltzmann sampler inspired by a quantum-inspired combinatorial optimization called simulated bifurcation (SB). This SB-inspired approach, which we name Langevin SB (LSB), enables parallelized sampling while maintaining accuracy comparable to MCMC. Furthermore, this is applicable not only to RBMs but also to BMs with general couplings. However, LSB cannot control the inverse temperature of the output Boltzmann distribution, which hinders learning and degrades performance. To overcome this limitation, we also developed an efficient method for estimating the inverse temperature during the learning process, which we call conditional expectation matching (CEM). By combining LSB and CEM, we establish an efficient learning framework for BMs with greater expressive power than RBMs. We refer to this framework as sampler-adaptive learning (SAL). SAL opens new avenues for energy-based generative modeling beyond RBMs.

I. INTRODUCTION

Boltzmann machines (BMs) are expressive generative models that capture complex dependencies and latent structures [1–5]. Their applications span diverse areas, including image recognition and restoration [3], anomaly detection [6], natural language processing [7, 8], and statistical and quantum physics [9–13]. Early developments in BMs laid the foundation for modern deep learning [14–18].

A BM is defined as an undirected neural network comprising visible units \mathbf{v} , which represent the observed data, and hidden units \mathbf{h} , which enhance the model’s expressive capacity [see Fig. 1(c)–(e)]. Both \mathbf{v} and \mathbf{h} are binary vectors of dimensions N_v and N_h , respectively, taking values in $\{-1, +1\}$, like Ising spins. The full state of the BM is denoted by an N -dimensional Ising vector $\mathbf{s} = (\mathbf{v}^T, \mathbf{h}^T)^T$, where $N = N_v + N_h$. The BM models a target distribution $P_D(\mathbf{v})$ using a marginal Boltzmann distribution $Q_\beta(\mathbf{v}|\mathbf{u}) = \sum_{\mathbf{h}} B_\beta(\mathbf{s}|\mathbf{u})$, where

$$B_\beta(\mathbf{s}|\mathbf{u}) = Z_\beta^{-1} e^{-\beta E(\mathbf{s}|\mathbf{u})}, \quad (1)$$

is a Boltzmann distribution with inverse temperature β , $Z_\beta = \sum_{\mathbf{s}} e^{-\beta E(\mathbf{s}|\mathbf{u})}$ is the partition function,

$$E(\mathbf{s}|\mathbf{u}) = -\frac{1}{2} \mathbf{s}^T \mathbf{J} \mathbf{s} - \mathbf{f} \cdot \mathbf{s}, \quad (2)$$

is the global energy function, \mathbf{J} is a weight matrix, \mathbf{f} is a bias vector, and $\mathbf{u} = (\mathbf{J}, \mathbf{f})$ denotes the model parameter set to be optimized (see Sec. IV A for details). Learning aims to minimize the Kullback-Leibler (KL) divergence $D_{\text{KL}}(P_D||Q_\beta) =$

$\sum_{\mathbf{v}} P_D(\mathbf{v}) \log \frac{P_D(\mathbf{v})}{Q_\beta(\mathbf{v}|\mathbf{u})}$ for \mathbf{u} , typically via gradient-based methods. Since the exact calculation of the gradients scales exponentially with the system size, it is standard to approximate the gradients using Boltzmann sampling, most commonly via Markov chain Monte Carlo (MCMC) techniques such as Gibbs sampling [20] or the Metropolis–Hastings algorithm [21, 22].

However, due to inherently sequential update rules, MCMC is slow and does not scale well to practical applications. Restricted BMs (RBMs) [23–25] provide a notable exception: their bipartite structure [see Fig. 1(d)] leads to conditional independence, which enables efficient parallel sampling (blocked Gibbs). This property underpins an efficient learning method called contrastive divergence (CD) and supports many practical applications [26]. In contrast, when intra-unit connections are introduced to increase expressive power, this advantage is lost. For example, semi-restricted BMs (SRBMs) [27–29][see Fig. 1(e)], which add interactions within the visible units to RBMs, require visible variables to be updated sequentially, substantially increasing computation time. Consequently, practical applications of more expressive BMs than RBMs remain scarce, and existing examples mostly rely on approximate learning methods, leading to performance reduction (see Refs. [27 and 29] and Supplementary Information).

To address this limitation, we introduce a novel Boltzmann sampler inspired by a quantum-inspired combinatorial optimization called simulated bifurcation (SB) [30–34]. We refer to this algorithm as Langevin SB (LSB). LSB enables parallel sampling even for BMs with general couplings, e.g., SRBMs, while maintaining the accuracy comparable to the most reliable method, namely sequential MCMC. However, LSB has a drawback: the inverse temperature of the output distribution, β_{eff} , is unknown and depends on the problem instance \mathbf{u} and sampler settings, like other samplers based on optimization machines or algorithms —such as D-Wave’s quan-

* kentaro.kubo.b91@mail.toshiba

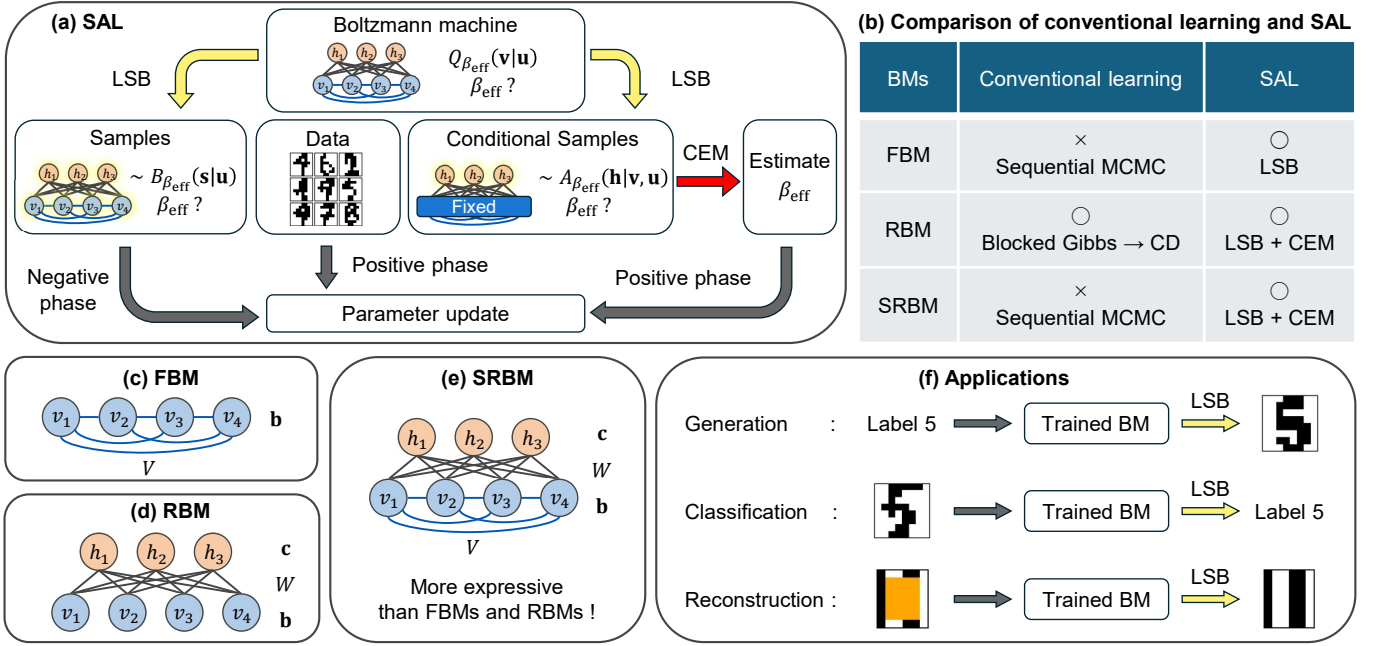


FIG. 1. **Overview of the sampler-adaptive learning (SAL) framework and model structures.** (a) Schematic of the SAL framework, which combines Langevin simulated bifurcation (LSB, yellow arrows) for fast parallel sampling and conditional expectation matching (CEM, red arrow) for efficient estimation of the effective inverse temperature β_{eff} . The parameter update is performed by gradient descent on the Kullback–Leibler (KL) divergence $D_{\text{KL}}(P_D || Q_{\beta_{\text{eff}}})$, where the gradient is given by the difference between the positive phase and the negative phase (see Sec. IV B). LSB generates both standard and conditional samples, respectively, from the Boltzmann distribution $B_{\beta_{\text{eff}}}(\mathbf{s}|\mathbf{u})$ for the negative phase and the conditional Boltzmann distribution $A_{\beta_{\text{eff}}}(\mathbf{h}|\mathbf{v}, \mathbf{u})$ (see Sec. IV C) for the positive phase. Here, sampled variables are highlighted in yellow. The negative phase is computed using only standard samples from $B_{\beta_{\text{eff}}}(\mathbf{s}|\mathbf{u})$, while the positive phase uses the data distribution P_D together with β_{eff} estimated via CEM from conditional samples drawn from $A_{\beta_{\text{eff}}}(\mathbf{h}|\mathbf{v}, \mathbf{u})$. (b) Comparison of learning methods: SAL (LSB + CEM) versus conventional MCMC-based learning. (c-e) Model structures: Each model consists of visible nodes v_i (blue circles, arranged in the lower row) and, if present, hidden nodes h_j (orange circles, arranged in the upper row). Edges represent pairwise interactions: blue lines between visible nodes indicate visible–visible interactions V_{ij} , and gray lines between visible and hidden nodes indicate visible–hidden interactions W_{ij} . The bias vectors for the visible and hidden nodes are denoted by \mathbf{b} and \mathbf{c} , respectively. (c) Fully visible Boltzmann machine (FBM): only visible nodes are present, and all visible nodes are mutually connected. (d) Restricted Boltzmann machine (RBM): both visible and hidden nodes are present; every visible node is connected to every hidden node, but there are no connections among visible nodes or among hidden nodes. (e) Semi-restricted Boltzmann machine (SRBM): both visible and hidden nodes are present; every visible node is connected to every hidden node, and all visible nodes are also mutually connected, but there are no connections among hidden nodes. (f) Examples of applications of BMs trained with SAL: image generation, classification, and reconstruction.

tum annealers [35–42], coherent Ising machines (CIM) [43–45], and simulated CIM (SimCIM) [46, 47]. Unless β_{eff} is accurately estimated or controlled, the learning process cannot proceed reliably. However, the standard approach for estimating β_{eff} —KL divergence minimization—is computationally prohibitive inside the learning loop [48]. Although alternative methods have been explored, they suffer from accuracy and stability issues [47–49], or rely on BMs without hidden variables, namely, fully-visible BMs (FBMs), [see Fig. 1(c)] sacrificing expressive power to circumvent β_{eff} estimation [50]. Thus, the use of fast parallelizable samplers, including LSB, for BM learning demands a scalable and accurate β_{eff} estimation method. Here, we also introduce such an efficient β_{eff} estimation method for SRBMs, which we name conditional expectation matching (CEM). CEM is parallelizable with LSB sampling process and provides accurate estimation of β_{eff} .

By combining LSB and CEM, we propose a new learning framework [see Fig. 1(a)], which enables efficient training not only of RBMs but also of FBMs and SRBMs [see

Fig. 1(c)–(e)], unlike conventional learning approaches [see Fig. 1(b)]. We term this framework as sampler-adaptive learning (SAL). Note that BMs that include interactions within the hidden units do not scale efficiently regardless of the sampler used [16], and thus SRBMs represent the most expressive BMs among those that can be practically trained. SAL is important as it enabled the efficient training of such SRBMs. We demonstrate that SAL-trained SRBMs outperform conventional methods in minimizing the training cost function on synthetic spin-glass datasets [51, 52]. Furthermore, we achieve high performance across multiple tasks: high-fidelity image generation and reconstruction on the Bars-and-Stripes dataset [3, 53], both unconditional and conditional image generation, and high classification accuracy on OptDigits [54] [see Fig. 1(f)]. Our findings highlight the practical and scalable nature of SAL, laying the groundwork for advancing energy-based generative modeling beyond RBMs.

II. RESULTS

A. Sampler-adaptive learning (SAL) framework

We first provide an overview of the SAL framework shown in Fig. 1(a), which enables scalable training of SRBMs [27, 28][see Fig. 1(e)]. The energy function is defined as follows:

$$E(\mathbf{s}|\mathbf{u}) = -\frac{1}{2}\mathbf{v}^T V \mathbf{v} - \mathbf{v}^T W \mathbf{h} - \mathbf{b} \cdot \mathbf{v} - \mathbf{c} \cdot \mathbf{h}, \quad (3)$$

where V (W) is a weight matrix between visible and visible units (between visible and hidden units), \mathbf{b} and \mathbf{c} are bias vectors for \mathbf{v} and \mathbf{h} , respectively, and $\mathbf{u} = (V, W, \mathbf{b}, \mathbf{c})$ denotes the set of model parameters. Since SRBMs encompass FBMs and RBMs as special cases, SAL is applicable to all three types of models [see Fig. 1(c)-(e)] that can be practically trained [16].

In conventional BM learning, the inverse temperature β of the model distribution $Q_\beta(\mathbf{u})$ is fixed, typically to 1. In contrast, SAL sets β to β_{eff} , the inverse temperature of the output distribution produced by LSB (see Sec. II A 1), which depends on \mathbf{u} and the sampling setting (see Sec. II A 2). As \mathbf{u} is updated during learning, β_{eff} also changes. Thus, SAL involves not only updating the learning parameters \mathbf{u} but also adapting the model function $Q_{\beta_{\text{eff}}}$ to the inverse temperature β_{eff} . This stands in sharp contrast to the conventional learning procedure, which updates only \mathbf{u} while keeping β (and consequently the model function Q_β) fixed. Learning is performed by gradient descent on $D_{\text{KL}}(P_D||Q_{\beta_{\text{eff}}})$. The gradient decomposes into a negative phase, defined as an expectation under the Boltzmann distribution $B_{\beta_{\text{eff}}}(\mathbf{s}|\mathbf{u})$, and a positive phase, defined using the data distribution P_D together with β_{eff} [see Sec. IV B for the details]. SAL employs LSB as a fast, parallelizable sampler for the negative phase and CEM as an efficient β_{eff} estimator for the positive phase [see Fig. 1(a) and Sec. IV B]. The remainder of this subsection provides details of LSB and CEM.

1. Langevin simulated bifurcation (LSB)

Several optimization machines and algorithms, such as D-Wave's quantum annealers, coherent Ising machines (CIM), and simulated CIM (SimCIM), have been shown to function effectively as Boltzmann samplers [35–47]. Inspired by these findings, we investigated the output distributions of another class of optimization algorithms, simulated bifurcation (SB) algorithms [30–34]. Our results show that special cases of conventional SB algorithms approximate the Boltzmann distribution to a nontrivial degree, but their sampling accuracy is substantially lower than that achieved by MCMC methods (see Supplementary Information). In this section, we propose a modified sampling algorithm that achieves sampling accuracy comparable to MCMC. We refer to this algorithm as Langevin Simulated Bifurcation (LSB), since its continuous limit resembles the celebrated continuous-variable sampler, Langevin Monte Carlo, whose stationary distribution is guaranteed to be the Boltzmann distribution [55, 56].

Similarly to discrete SB (dSB) [31], LSB is based on the following equations of motion for positions x_i and momenta y_i corresponding to s_i in the general global energy function $E(\mathbf{s}|\mathbf{u})$:

$$\dot{y}_i = - \left. \frac{\partial E(\mathbf{x}|\mathbf{u})}{\partial x_i} \right|_{\mathbf{x}=\mathbf{s}}, \quad (4)$$

$$\dot{x}_i = y_i, \quad (5)$$

where the dots denote time derivatives. Equations (4) and (5) are solved with the symplectic Euler method [57]:

$$y_i(k+1) = y_i(k) + \left\{ \sum_{j=1}^N J_{ij} \text{sgn}[x_j(k)] + f_i \right\} \Delta, \quad (6)$$

$$x_i(k+1) = x_i(k) + y_i(k+1)\Delta, \quad (7)$$

where Δ is the time step and $k \in \{0, \dots, M\}$ denotes iteration. To improve sampling accuracy, at the end of each iteration, LSB applies discretization and stochastic initialization to x_i and y_i , respectively:

$$x_i \rightarrow \text{sgn}(x_i), \quad (8)$$

$$y_i \rightarrow \xi_i \sim \mathcal{N}(0, \sigma), \quad (9)$$

where ξ_i is a stochastic variable drawn from a Gaussian distribution $\mathcal{N}(\mu, \sigma)$ with mean $\mu = 0$ and standard deviation σ , and the notation \sim indicates that the variable on the left-hand side follows the distribution on the right-hand side. Here, Δ and σ are the only hyperparameters of LSB. Note that the update rule inherits the properties of the conventional SB algorithm and can be implemented in parallel for each component. In this work, x_i and y_i are initialized by sampling uniformly from $\{-1, 1\}$ and from $N(0, \sigma)$ using the same σ as in the update rule, respectively, though other choices are possible in general. After M iterations of the above updates, the resulting \mathbf{x} provides a sample of $\mathbf{s} = \text{sgn}(\mathbf{x})$; executing this procedure L times, we obtain a sampled Ising vector set $\{\mathbf{s}^{(l)} | l = 1, \dots, L\}$.

To assess the sampling performance of LSB, we evaluated its accuracy against conventional Gibbs sampling (MCMC) at $\beta = 1$ on random SRBMs with $N_v = 10$ and $N_h = 5$, using $M = 100$ iterations for LSB and the same M Monte Carlo steps for Gibbs sampling. Edge weight V_{ij} and W_{ij} were sampled from $\mathcal{N}\left(0, \frac{2}{\sqrt{N}}\right)$ with $N = N_v + N_h = 15$, and bias b_i and c_i were set to zero. Sampling accuracy was defined as the KL divergence $D_{\text{KL}}(P_S||B_{\beta_{\text{eff}}})$, where $P_S(\mathbf{s}) = \frac{1}{L} \sum_{l=1}^L \delta(\mathbf{s} - \mathbf{s}^{(l)})$ represents the empirical distribution of the sampled Ising vectors, and $\delta(\mathbf{x}) = 1$ if $\mathbf{x} = \mathbf{0}$ and 0 otherwise. The effective inverse temperature β_{eff} was determined self-consistently by KL divergence minimization [48]: $\beta_{\text{eff}} = \text{argmin}_\beta D_{\text{KL}}(P_S||B_\beta)$. We initialized β at 1 and performed the minimization over $[0, \infty)$ using the L-BFGS-B method implemented in `scipy.optimize.minimize` [58].

Figure 2 shows the sampling accuracy $D_{\text{KL}}(P_S||B_{\beta_{\text{eff}}})$ and the corresponding β_{eff} values for 10 random instances. We fixed Δ at 1 and optimized σ from the candidate set $\sigma^{-2} \in \{0.5, 0.6, \dots, 1.9, 2.0\}$ to maximize LSB sampling accuracy for each instance. LSB outperformed Gibbs sampling in

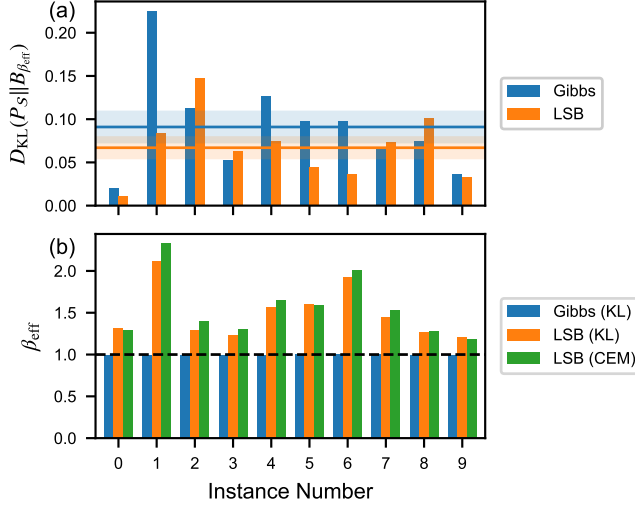


FIG. 2. **Sampling accuracy and effective inverse temperature for LSB and Gibbs sampling:** (a) Sampling accuracy $D_{\text{KL}}(P_S || B_{\beta_{\text{eff}}})$ for LSB and Gibbs sampling across 10 random instances of SRBM with $N_v = 10$ and $N_h = 5$. For each instance, Δ was fixed at 1 and σ was optimized from the candidate set $\sigma^{-2} \in \{0.5, 0.6, \dots, 2.0\}$ to maximize LSB sampling accuracy. Horizontal lines and shaded regions indicate the means KL divergence and their standard errors: 0.09 ± 0.02 for Gibbs and 0.07 ± 0.01 for LSB. (b) The effective inverse temperature β_{eff} for the output distribution produced by each sampler. For Gibbs sampling, β_{eff} was estimated by KL-divergence minimization. For LSB, β_{eff} was estimated by both KL-divergence minimization and CEM.

6 out of 10 instances based on the sampling accuracy metric $D_{\text{KL}}(P_S || B_{\beta_{\text{eff}}})$. Across all 10 instances, the mean $D_{\text{KL}}(P_S || B_{\beta_{\text{eff}}})$ (\pm standard error) was 0.09 ± 0.02 for Gibbs and 0.07 ± 0.01 for LSB. Taking the errors into account, LSB demonstrates performance comparable to or even better than Gibbs sampling. Furthermore, while Gibbs sampling does not allow parallel updates of visible variables in SRBMs, LSB enables simultaneous updates of all variables, providing a significant advantage in computational speed for large-scale problems. We use LSB for SAL in Sec. II B [see also Fig. 1(a)-(b)].

2. Conditional expectation matching (CEM)

Figure 2(b) shows that the effective inverse temperature β_{eff} estimated by KL-divergence minimization varies across instances for LSB sampling (orange), whereas Gibbs sampling consistently yields $\beta_{\text{eff}} \simeq 1$ (blue). Estimating the unknown β_{eff} is essential for successful learning (see Sec. IV B). However, the conventional approach based on KL-divergence minimization [48] scales exponentially with the system size N , making it intractable for practical problems. Thus, the instance-dependent variability of β_{eff} in LSB output distributions poses a significant challenge to BM learning with LSB. To overcome this, we propose a new and efficient β_{eff} estimation method: conditional expectation matching (CEM), as

detailed below.

In a Boltzmann distribution $B_{\beta_{\text{eff}}}(\mathbf{s}|\mathbf{u})$ of an SRBM, hidden variables are conditionally independent when the visible variables \mathbf{v} are fixed to a condition vector \mathbf{r} . This property allows analytical expressions for their conditional expectations:

$$\begin{aligned} \langle h_j \rangle_{\mathbf{r}, \beta_{\text{eff}}} &:= \sum_{\mathbf{h}} h_j A_{\beta_{\text{eff}}}(\mathbf{h}|\mathbf{v}, \mathbf{u}) \delta(\mathbf{v} - \mathbf{r}), \\ &= \tanh \left\{ \beta_{\text{eff}} \left(c_j + \sum_{i=1}^{N_v} r_i W_{ij} \right) \right\}, \end{aligned} \quad (10)$$

where

$$A_{\beta_{\text{eff}}}(\mathbf{h}|\mathbf{v}, \mathbf{u}) := \frac{B_{\beta_{\text{eff}}}(\mathbf{s}|\mathbf{u})}{\sum_{\mathbf{h}} B_{\beta_{\text{eff}}}(\mathbf{s}|\mathbf{u})}, \quad (11)$$

is a conditional Boltzmann distribution (see also Sec. IV C). On the other hand, $\langle h_j \rangle_{\mathbf{r}, \beta_{\text{eff}}}$ can also be directly obtained by conditional LSB sampling (see Sec. IV C). Hereafter, this sampling-based estimation of $\langle h_j \rangle_{\mathbf{r}, \beta_{\text{eff}}}$ is denoted by $\langle h_j \rangle_{\mathbf{r}, C}$. We estimate β_{eff} by minimizing the squared difference between $\langle h_j \rangle_{\mathbf{r}, C}$ and the right-hand side of Eq. (10) across all hidden units:

$$\beta_{\text{eff}} = \text{argmin}_{\beta > 0} F_{\mathbf{r}}(\beta), \quad (12)$$

$$F_{\mathbf{r}}(\beta) := \sum_{j=1}^{N_h} \left\{ \langle h_j \rangle_{\mathbf{r}, C} - \tanh \left[\beta \left(c_j + \sum_{i=1}^{N_v} r_i W_{ij} \right) \right] \right\}^2. \quad (13)$$

The minimization is performed similarly to the above KL-divergence minimization. This procedure, termed conditional expectation matching (CEM), leverages consistency between conditionally sampled expectations $\langle h_j \rangle_{\mathbf{r}, C}$ and analytical conditional expectations expressed as a function of β_{eff} [the right-hand side of Eq. (10)]. CEM can be executed in parallel with full-system sampling to approximate $B_{\beta_{\text{eff}}}(\mathbf{s}|\mathbf{u})$, in sharp contrast to conventional β_{eff} estimators [45, 47–49]. Furthermore, the conditional sampling cost to compute $\langle h_j \rangle_{\mathbf{r}, C}$ is lower than full-system sampling. Therefore, CEM does not become a bottleneck during learning. The condition vector \mathbf{r} can be randomly generated or selected from the dataset during learning, but is not restricted to these choices.

In Fig. 2(b), we compare β_{eff} estimated by CEM (green) with that obtained by KL-divergence minimization (orange) for LSB output distributions. For CEM, each component of the condition vectors \mathbf{r} was uniformly sampled from $\{-1, 1\}$. The mean signed relative error between them across 10 instances is approximately 3.6%. Comparisons with other inverse-temperature estimation methods, including modified versions of CEM (CEM- n), are provided in the Supplementary Information.

Thus, CEM enables accurate inverse temperature estimation. Moreover, because it is parallelizable with LSB sampling, it does not become a bottleneck in training, unlike the KL-based estimation [48]. By leveraging inverse temperature estimation through CEM in learning, we overcome the computational difficulty of the positive phase (see Sec. IV B and Ref. 50).

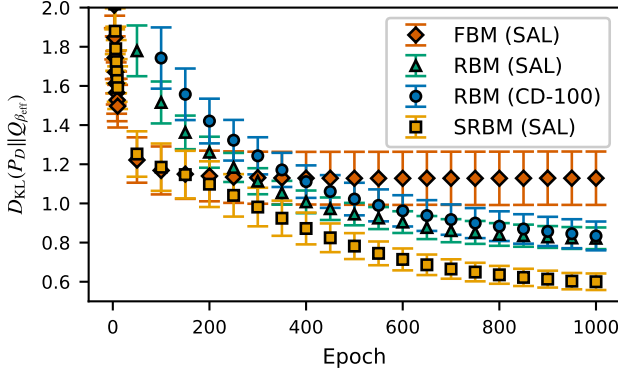


FIG. 3. **Learning performance on the 3-spin model:** The vertical axis shows the cost function $D_{\text{KL}}(P_D||Q_\beta)$, and the horizontal axis indicates training epochs. Four models are compared: FBMs, RBMs, and SRBMs trained using SAL; RBMs with $\beta = 1$ trained using CD-100. The number of hidden variables N_h for both RBMs and SRBMs was set to 5. Each point represents the mean over 10 independent instances, and error bars denote the standard error. Lower $D_{\text{KL}}(P_D||Q_\beta)$ values indicate closer agreement between Q_β and P_D .

B. Experiments

In this subsection, we apply SAL to train SRBMs on three distinct datasets, to demonstrate its scalability and effectiveness. The target distributions $P_D(\mathbf{v})$ are set as the empirical distribution of each dataset $\{\mathbf{v}^{(d)}|d=1,\dots,D\}$, where each data point $\mathbf{v}^{(d)}$ is an N_v -dimensional Ising vector: $P_D(\mathbf{v}) = \frac{1}{D} \sum_{d=1}^D \delta(\mathbf{v} - \mathbf{v}^{(d)})$. Details of each dataset and the training settings are provided in Sec. IV D.

1. Learning performance on the 3-spin model

We first use a dataset sampled from the exact Boltzmann distribution of a 3-spin model [51, 52]. The 3-spin model is an Ising system with random three-body interactions (see Sec. IV D) and has a highly rugged energy landscape. Consequently, the training data, drawn from its Boltzmann distribution, exhibit a nontrivial overlap distribution characterizing spin-glass systems (see Supplementary Information). To allow exact computation of the cost function $D_{\text{KL}}(P_D||Q_\beta)$ and enable quantitative comparison with conventional methods, we restricted N_v to 10. We prepared 10 independent instances to ensure statistically reliable performance evaluation.

Figure 3 compares the learning performance of four approaches: FBMs, RBMs and SRBMs trained with SAL (see Sec. IV B), and RBMs with $\beta = 1$ trained via contrastive divergence-100 (CD-100) [26]. Here, CD-100 means that the initial state is set to one of the data vectors and that 100 Monte Carlo steps of blocked Gibbs sampling (MCMC) are performed. The choice of 100 was made to match LSB sampling steps, $M = 100$ (see Sec. IV D for details of parameter setting). FBMs are fully connected Boltzmann machines without hidden variables ($N_h = 0$) [see Fig. 1(c)]. The number

of hidden variables N_h for both RBMs and SRBMs [see Fig. 1(d)-(e)] was set to 5. All the four approaches allow parallel sampling.

Among the four models, FBMs exhibited the poorest performance [highest $D_{\text{KL}}(P_D||Q_\beta)$]. This is natural because the 3-spin model includes non-pairwise (three-body) interactions that cannot be captured by FBMs, which rely solely on pairwise couplings. Introducing hidden variables, RBMs enabled the representation of higher-order correlations, leading to superior performance compared to FBMs. The observation that RBMs trained using SAL exhibit performance comparable to, or even surpassing, RBMs trained with CD-100 within the standard error suggests that SAL constitutes an effective learning strategy. Furthermore, SRBMs consistently achieved lower values of the cost function than RBMs across epochs. The difference between SRBMs and RBMs remained statistically significant even when considering the standard error, confirming the robustness of SRBM's advantage over RBMs. We also confirmed that SRBMs trained by replacing CEM in SAL with other computationally light but inaccurate inverse temperature estimation methods (maximum log-pseudo-likelihood estimation: MLPL [48, 49]) or by using CD with damped mean-field iterations [27] resulted in significantly lower performance compared to SRBMs trained with SAL (see Supplementary Information for details). This suggests that learning SRBMs, enabled by SAL, provides a distinct advantage, particularly for modeling highly rugged energy landscapes as exemplified by spin-glass systems.

2. Generative and reconstruction performance on the BAS dataset

We next consider the synthetic bars-and-stripes (BAS) dataset, consisting of binary images with horizontal and vertical stripe patterns (see Refs. [3] and [53]). We constructed a 7×6 BAS dataset with 192 distinct patterns (all possible patterns), split into $D = 96$ training and $D_{\text{Test}} = 96$ test samples (see Sec. IV D). While exact computation of $D_{\text{KL}}(P_D||Q_\beta)$ was possible for the 3-spin model with $N_v = 10$, it becomes challenging for the 7×6 BAS dataset ($N_v = 42$) due to the exponential growth of the state space. Therefore, here we focus on demonstrating the generative and reconstruction capabilities of SRBMs ($N_h = 21$) trained with SAL on the 7×6 BAS dataset, without computing $D_{\text{KL}}(P_D||Q_\beta)$. Training settings are detailed in Sec. IV D.

The generative capabilities are shown in Fig. 4. The SRBM was trained via SAL on $D = 96$ BAS patterns [panel (a) shows randomly selected 36 ones], and at various training epochs, 36 samples were generated by LSB from the trained SRBM [panels (b)–(f)]. As training progressed, the SRBM rapidly captured the essential features of both horizontal and vertical stripes, and at 6000 epochs [panel (f)] generated only valid BAS patterns without misgeneration.

Reconstruction experiment results shown in Fig. 5 further demonstrate the robustness of SAL. Here, we masked a central 5×4 block of each test image [Fig. 5(a)], resulting in a collapsed image with 47.6% of pixels missing (shown in orange) [Fig. 5(b)]. By fixing the visible variables of the SRBM

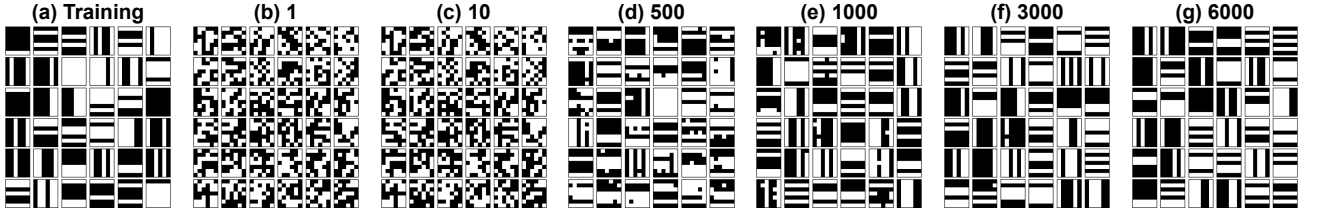


FIG. 4. **Generative performance on the BAS dataset:** (a) 36 randomly selected training samples. (b)–(g) 36 samples generated by the trained SRBM with LSB after 1, 10, 500, 1000, 3000, and 6000 training epochs, respectively.

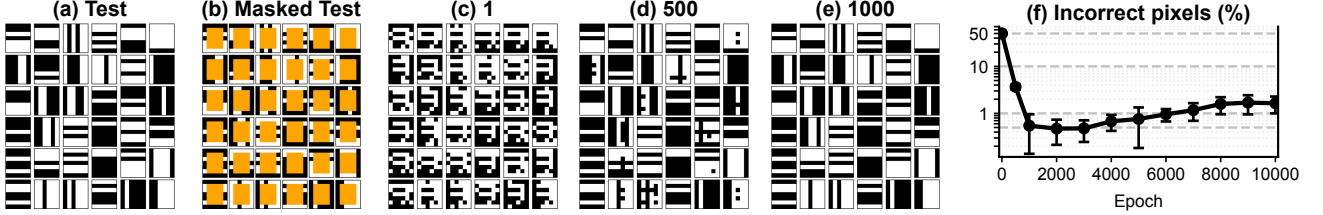


FIG. 5. **Reconstruction performance on the BAS dataset:** (a) 36 randomly selected test samples. (b) The same samples with a central 5×4 block masked (47.6% of pixels missing, shown in orange). (c)–(e) Reconstructions of (b) using the trained SRBM at 1, 500, and 1000 epochs, respectively, obtained by conditional LSB sampling. (f) The ratio of incorrect pixels per reconstruction as a function of training epoch. Each data point represents the mean over 10 independent runs with different random initializations of \mathbf{u} ; error bars indicate the standard deviation

corresponding to the intact pixels in panel (b) to their observed values, we inferred the masked pixel values via conditional sampling (see Fig. 1(f) and Sec. IV C). After 1000 epochs of learning, almost all patterns were successfully reconstructed by leveraging the learned distribution [Fig. 5(e)]. Fig. 5(f) shows the fraction of incorrect pixels per reconstruction, evaluated across all $D_{\text{Test}} = 96$ test samples. This fraction rapidly dropped from 50.0% (corresponding to random restoration) at 1 epoch to 0.5% at 1000–3000 epochs, indicating near-perfect reconstruction across all test samples. As training progressed beyond 3000 epochs, the fraction gradually increased to around 2%, suggesting potential overfitting with excessive training. Importantly, these results demonstrate that the SRBM trained with SAL learns the underlying distribution rather than memorizing individual samples, enabling robust and generalizable reconstruction even under substantial pixel loss.

3. Generative and classification performance on the OptDigits dataset

The OptDigits dataset consists of 8×8 images of handwritten digits and their class labels [54]. We flattened and binarized the images, and represented the data class using one-hot encoding, resulting in $D = 3823$ training samples and $D_{\text{Test}} = 1797$ test samples with $N_v = 74$ visible variables. Details of preprocessing are provided in Sec. IV D. Compared to the 3-spin model and BAS dataset, OptDigits has approximately 7.4-fold and 1.8-fold larger N_v , respectively, providing a more challenging and realistic benchmark. In the following, we demonstrate that the SRBM trained with SAL on OptDigits captures the data distribution for generative modeling and

enables accurate image classification using the learned representation. Training settings are detailed in Sec. IV D.

The generative performance is shown in Fig. 6. The SRBM was trained via SAL on $D = 3823$ digit images [panel (a) shows 64 randomly selected samples], and at various training epochs, 64 samples were generated by LSB sampling from the trained SRBM [panels (b)–(e)]. While samples at 1 epoch [panel (b)] exhibited little recognizable structure, subsequent epochs revealed a progressive emergence of digit-specific patterns consistent with the training data [panels (c)–(e)]. By 10 epochs [panel (c)], the generated images began to resemble the target digits, and by 500 and 3000 epochs [panels (d) and (e)], most samples captured the essential characteristics of handwritten digits and were visually recognizable.

We further evaluated the ability to perform conditional generation by fixing the class label \mathbf{C} to the desired value and sampling the image variables \mathbf{I} using LSB [see Fig. 1(f), Sec. IV C, and IV D]. Figure 7 illustrates the results. For each $n \in \{0, 1, \dots, 9\}$, panel (a- n) shows 16 randomly selected test images of digit n , and panel (b- n) shows 16 samples generated from the SRBM after 3000 training epochs by conditional LSB sampling with the digit class n . Most of the generated images exhibited clear digit structures consistent with the specified condition, demonstrating that the SRBM successfully reproduced the overall data distribution and enabled class-conditional sample generation.

Finally, we evaluated the capability of the learned SRBM to perform image classification. For each test sample $d \in \{1, \dots, D_{\text{Test}}\}$, the visible variables corresponding to the image \mathbf{I} were fixed to their observed values $\mathbf{I}^{(d)}$, and conditional LSB sampling of \mathbf{C} was performed to infer the class label $\mathbf{C}^{(d)}$ (see Sec. IV C and Sec. IV D). The average label vector computed from conditionally sampled labels for each image

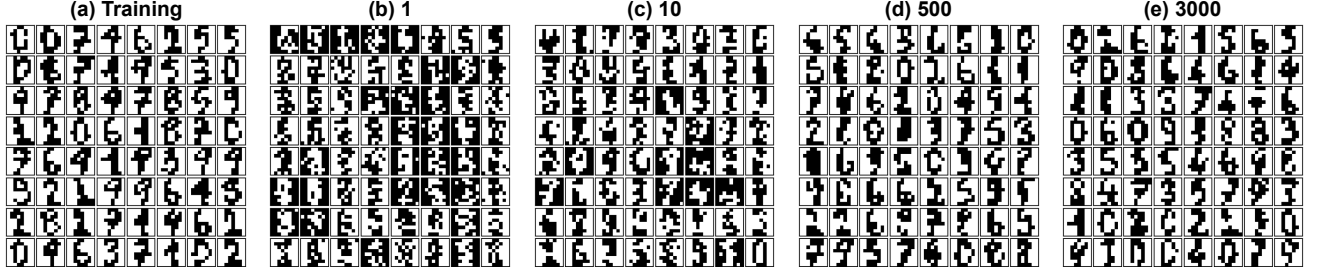


FIG. 6. **Generative performance on the OptDigits dataset:** (a) 64 randomly selected training samples. (b)–(e) 64 samples generated by the trained SRBM with LSB at 1, 10, 500, and 3000 training epochs, respectively.

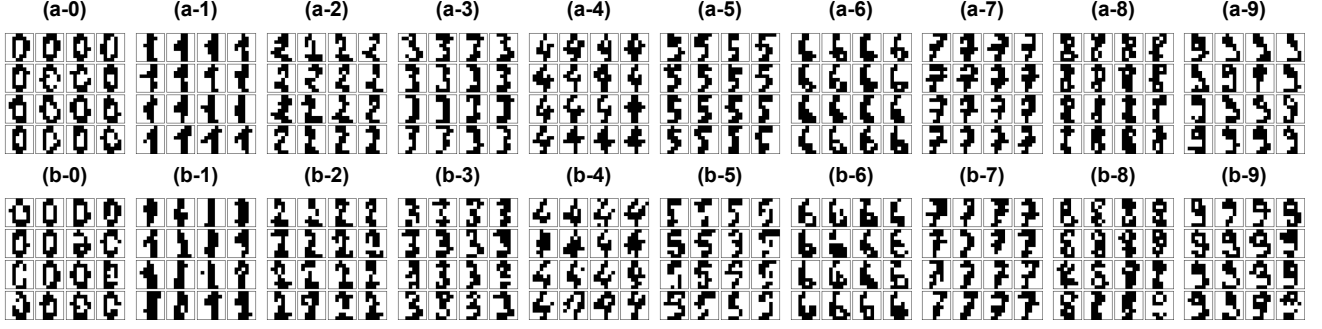


FIG. 7. **Class-specified generation on the OptDigits dataset:** (a-n) 16 randomly selected test samples for digit $n \in \{0, 1, \dots, 8, 9\}$. (b-n) 16 samples generated by conditional LSB sampling from the trained SRBM at 3000 epochs, conditioned on class label $n \in \{0, 1, \dots, 8, 9\}$.

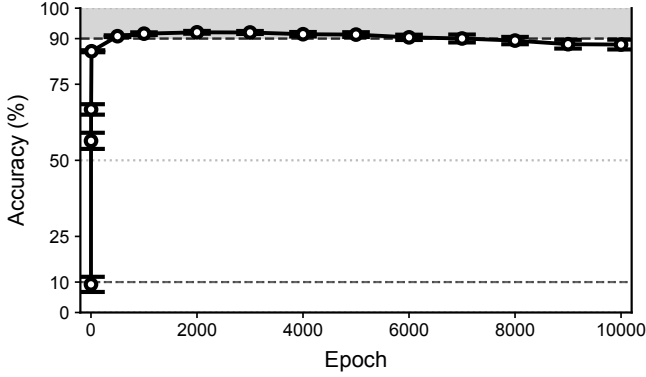


FIG. 8. **Classification accuracy on the OptDigits dataset:** The vertical axis shows the classification accuracy (%), and the horizontal axis indicates training epochs. Each data point represents the mean over 10 independent runs with different random initializations of \mathbf{u} ; error bars indicate the standard deviation. The shaded region marks accuracy above 90%, and the horizontal dashed lines indicate the 10% baseline (random guessing) and the 90% reference line.

d was transformed into a one-hot representation $\tilde{\mathbf{C}}$ by setting +1 for the component with the highest value and -1 for all others. Classification was deemed correct when this one-hot representation $\tilde{\mathbf{C}}$ matched the true class label $\mathbf{C}^{(d)}$. Figure 8 shows that the classification accuracy improved substantially with training, rapidly reaching nearly 90% at 500 epochs from

nearly 10% (corresponding to random guessing in a 10-class problem) before training, underscoring the effectiveness of the proposed learning approach.

III. DISCUSSION

Our results highlight the potential of SAL to unlock expressive modeling capabilities in BMs beyond RBMs, such as SRBMs, which have previously been considered impractical. While our work has focused exclusively on SRBMs, future research could explore extensions to deeper architectures and other energy-based models for large-scale applications. Furthermore, SAL is expected to remain effective with other parallel non-MCMC samplers in place of LSB. Exploring these possibilities could open multiple avenues for future research.

We have focused on SRBMs, but LSB also enables fast and accurate sampling for more general models, including those with intra-unit couplings among hidden variables (see Supplementary Information). Remarkably, our results suggest that LSB may even surpass MCMC in sampling accuracy for many instances of complex spin-glass problems with rugged energy landscapes. As mentioned, the continuous limit of LSB resembles Langevin Monte Carlo [55, 56], whose output distribution is guaranteed to be the Boltzmann distribution. However, the theoretical basis for why LSB can well approximate the discrete Boltzmann distribution remains unclear, repre-

senting an important avenue for future research. Furthermore, developing systematic or automated strategies for hyperparameter selection in LSB is another open challenge. While this work has mainly addressed the parallelizability of samplers, elucidating their relaxation properties is also an important subject for future research.

For RBMs, not only CEM but also a variant of CEM exploiting the independence of visible variables can also be employed. However, because RBMs allow efficient blocked Gibbs sampling, situations where non-MCMC samplers—and thus β_{eff} estimation—are truly advantageous are relatively rare. CEM demonstrates its true value when applied to models beyond RBMs, where parallel MCMC sampling is not feasible. While our experiments demonstrate that CEM provides sufficiently accurate estimates of the effective inverse temperature β_{eff} for practical training, the necessary conditions for its reliability and the factors affecting estimation accuracy remain unclear. Further investigation into the statistical properties and convergence behavior of CEM remains an important direction for future research.

IV. METHODS

A. Boltzmann machines

The visible units are defined as $\mathbf{v} = (v_1, \dots, v_{N_v})^T$, and the hidden units as $\mathbf{h} = (h_1, \dots, h_{N_h})^T$. The full state of the BM is represented as $\mathbf{s} = (\mathbf{v}^T, \mathbf{h}^T)^T$, an N -dimensional Ising vector with $N = N_v + N_h$. The BM models a target distribution $P_D(\mathbf{v})$ within a family of marginal Boltzmann distributions

$$Q_\beta(\mathbf{v}|\mathbf{u}) = \sum_{\mathbf{h}} B_\beta(\mathbf{s}|\mathbf{u}), \quad (14)$$

where $B_\beta(\mathbf{s}|\mathbf{u}) = Z_\beta^{-1} e^{-\beta E(\mathbf{s}|\mathbf{u})}$ is a Boltzmann distribution of \mathbf{s} with an inverse temperature value β , $Z_\beta = \sum_{\mathbf{s}} e^{-\beta E(\mathbf{s}|\mathbf{u})}$ is a partition function, $E(\mathbf{s}|\mathbf{u}) = -\frac{1}{2} \mathbf{s}^T J \mathbf{s} - \mathbf{f} \cdot \mathbf{s}$ is a global energy function, J is a $(N \times N)$ -dimensional weight matrix with $J_{ii} = 0$ and $J_{ij} = J_{ji} \in \mathbb{R}$ for $i \neq j$, \mathbf{f} is a N -dimensional bias vector with $f_i \in \mathbb{R}$, and $\mathbf{u} = (J, \mathbf{f})$ denotes the model parameter set to be optimized. Throughout this paper, for an Ising vector \mathbf{S} , the notation $\sum_{\mathbf{S}}$ denotes the summation over all configurations of \mathbf{S} . For SRBMs, RBMs, and FBMs, the parameter set $\mathbf{u} = (J, \mathbf{f})$ can be denoted as $\mathbf{u} = (V, W, \mathbf{b}, \mathbf{c})$, $(W, \mathbf{b}, \mathbf{c})$, and (V, \mathbf{b}) , respectively, where V (W) is a weight matrix between visible and visible units (between visible and hidden units), \mathbf{b} and \mathbf{c} are bias vectors for \mathbf{v} and \mathbf{h} , respectively [see Fig. 1(c)-(e)].

B. Learning rule of SAL

Learning aims to minimize the Kullback-Leibler (KL) divergence between the target distribution P_D and Q_β

$$D_{\text{KL}}(P_D || Q_\beta) = \sum_{\mathbf{v}} P_D(\mathbf{v}) \log \frac{P_D(\mathbf{v})}{Q_\beta(\mathbf{v}|\mathbf{u})}, \quad (15)$$

typically via gradient-based methods. In SAL, where the inverse temperature β is set to β_{eff} , the inverse temperature of the output distribution produced by the sampler, the parameters of SRBMs are updated as follows:

$$V_{ij}(k+1) = V_{ij}(k) - \eta [\langle v_i v_j \rangle_D - \langle v_i v_j \rangle_{\beta_{\text{eff}}}], \quad (16)$$

$$W_{ij}(k+1) = W_{ij}(k) - \eta \left\{ \left\langle v_i \tanh \left[\beta_{\text{eff}} \left(c_j + \sum_{i=1}^{N_v} v_i W_{ij} \right) \right] \right\rangle_D - \langle v_i h_j \rangle_{\beta_{\text{eff}}} \right\}, \quad (17)$$

$$b_i(k+1) = b_i(k) - \eta [\langle v_i \rangle_D - \langle v_i \rangle_{\beta_{\text{eff}}}], \quad (18)$$

$$c_j(k+1) = c_j(k) - \eta \left\{ \left\langle \tanh \left[\beta_{\text{eff}} \left(c_j + \sum_{i=1}^{N_v} v_i W_{ij} \right) \right] \right\rangle_D - \langle h_j \rangle_{\beta_{\text{eff}}} \right\}, \quad (19)$$

where k denotes the learning step, $\eta > 0$ is the β_{eff} -renormalized learning rate [50], $\langle \bullet \rangle_D$ indicates the expectation value under the data distribution $P_D(\mathbf{v})$, and $\langle \bullet \rangle_{\beta_{\text{eff}}}$ indicates the expectation value under the Boltzmann distribution $B_{\beta_{\text{eff}}}(\mathbf{s})$ with inverse temperature β_{eff} . The terms defined by $\langle \bullet \rangle_D$ are referred to as the positive phase, whereas those defined by $\langle \bullet \rangle_{\beta_{\text{eff}}}$ are referred to as the negative phase. These update rules assume that variations in β_{eff} are negligible compared to changes in \mathbf{u} . The negative phase is computed using

LSB as follows:

$$\langle \bullet \rangle_{\beta_{\text{eff}}} \simeq \sum_{l=1}^L P_S(\mathbf{s}) \bullet, \quad (20)$$

where $P_S(\mathbf{s}) = \frac{1}{L} \sum_{l=1}^L \delta(\mathbf{s} - \mathbf{s}^{(l)})$ represents the empirical distribution of Ising vectors $\{\mathbf{s}^{(l)} | l = 1, \dots, L\}$ sampled by LSB. Thus, the negative phase does not require explicit information about β_{eff} . On the other hand, computing the positive phase

associated with the hidden units [Eqs. (17) and (19)] requires the effective inverse temperature β_{eff} , which is estimated using CEM.

Setting the initial values of V_{ij} to zero and updating only W_{ij} , b_i , and c_j reduces the update rule to that of an RBM. Similarly, setting $N_h = 0$ and updating only V_{ij} and b_i reduces the update rule to that of an FBM. In the FBM case, only Eqs. (16) and (18) remain, and β_{eff} estimation is no longer required. The FBM version of SAL has already been reported as the Gray-box algorithm [50]. That study reported that when hidden variables are present, computing the positive phase becomes difficult, and consequently they restricted their approach to FBMs, which can be trained without explicit knowledge of β_{eff} . SAL overcomes this challenge by leveraging SRBM's (and RBM's) structure together with CEM for efficient β_{eff} estimation, enabling scalable learning without sacrificing expressive power.

C. Conditional sampling

In CEM and applications such as, image reconstruction, conditional generation, and classification [see Fig. 1(a)-(b)], conditional sampling, which fixes a subset of variables while sampling the others, is often required. This is relatively straightforward with sequential MCMC methods; however, its implementation in non-MCMC samplers that perform parallel updates requires careful consideration. To achieve conditional sampling, Ref. [50] employed approaches that impose strong biases on the fixed variables in a D-Wave's quantum annealer. However, because both the inverse temperature and sampling accuracy depend strongly on \mathbf{u} in LSB sampling, such methods raise concerns about potential changes in output characteristics when applied to LSB-based sampling. Therefore, we adopt an alternative strategy as described below.

For simplicity, we consider the case where a subset of visible variables \mathbf{v}_f is fixed. This formulation covers all cases of conditional sampling in this study, and fixing more general variables, including hidden ones, can be formulated similarly. In this scenario, the energy of SRBMs, up to an additive constant, takes the following form:

$$E(\mathbf{v}_v, \mathbf{h} | \mathbf{v}_f, \mathbf{u}) = -\frac{1}{2} \mathbf{v}_v^T V_{vv} \mathbf{v}_v - \mathbf{v}_v^T W_v \mathbf{h} - (\mathbf{b}_v^T + \mathbf{v}_f^T V_{fv}) \mathbf{v}_v - (\mathbf{c}^T + \mathbf{v}_f^T W_f) \mathbf{h}. \quad (21)$$

Here, \mathbf{v}_v denotes the unfixed visible variables, $V_{\mu\rho}$ (W_μ) is a weight matrix between \mathbf{v}_μ and \mathbf{v}_ρ (between \mathbf{v}_μ and \mathbf{h}) for $\mu, \rho \in \{v, f\}$, \mathbf{b}_v is a bias vector of \mathbf{v}_v . The energy $E(\mathbf{v}_v, \mathbf{h} | \mathbf{v}_f, \mathbf{u})$ can be regarded as that of a conditional Boltzmann machine, $E(\mathbf{s}' | \mathbf{u}')$, defined over $\mathbf{s}' = (\mathbf{v}_v^T, \mathbf{h}^T)^T$ with parameter set $\mathbf{u}' = (J', \mathbf{f}')$. Here, $\mathbf{f}' = (\mathbf{b}'^T, \mathbf{c}'^T)^T$, $\mathbf{b}' = \mathbf{b}_v + (\mathbf{v}_f^T V_{fv})^T$, $\mathbf{c}' = \mathbf{c} + (\mathbf{v}_f^T W_f)^T$, and

$$J' = \begin{pmatrix} V_{vv} & W_v \\ W_v^T & O_h \end{pmatrix}, \quad (22)$$

where O_h is an $(N_h \times N_h)$ -dimensional zero matrix.

By executing LSB sampling for $E(\mathbf{s}' | \mathbf{u}')$ using the same hyperparameters as those used for sampling $B_{\beta_{\text{eff}}}(\mathbf{s} | \mathbf{u})$, we obtain a conditionally sampled Ising vector set $\{\mathbf{s}'^{(l)} | l = 1, \dots, L'\}$. For the sake of simplicity in this study, we assumed $L' = L$. We expect the empirical distribution $P_{S'}(\mathbf{s}') = \frac{1}{L'} \sum_{l'=1}^{L'} \delta(\mathbf{s}' - \mathbf{s}'^{(l')})$ to approximate the Boltzmann distribution of the conditional Boltzmann machine $B_{\beta_{\text{eff}}}(\mathbf{s}' | \mathbf{u}')$, which shares the same inverse temperature β_{eff} as $B_{\beta_{\text{eff}}}(\mathbf{s} | \mathbf{u})$. This conjecture is supported by numerical results obtained under the same conditions as Fig. 2(b), in which we confirmed that $D_{\text{KL}}[P_{S'}(\mathbf{s}') || B_{\beta_{\text{eff}}}(\mathbf{s}' | \mathbf{u}')] \ll D_{\text{KL}}[P_S(\mathbf{s}) || B_{\beta_{\text{eff}}}(\mathbf{s} | \mathbf{u})]$.

Note that $B_{\beta_{\text{eff}}}(\mathbf{s}' | \mathbf{u}')$ corresponds to the conditional Boltzmann distribution of the original Boltzmann machine:

$$A_{\beta_{\text{eff}}}(\mathbf{s}' | \mathbf{v}_f, \mathbf{u}) = \frac{B_{\beta_{\text{eff}}}(\mathbf{s}' | \mathbf{u})}{\sum_{\mathbf{v}_v} \sum_{\mathbf{h}} B_{\beta_{\text{eff}}}(\mathbf{s} | \mathbf{u})}. \quad (23)$$

In CEM, we set \mathbf{v}_f to \mathbf{v} and \mathbf{s}' to \mathbf{h} . We then compute sampling-based estimation of $\langle h_j \rangle_{\mathbf{r}, \beta_{\text{eff}}}$,

$$\langle h_j \rangle_{\mathbf{r}, C} := \sum_{\mathbf{h}} h_j P_{S'}(\mathbf{h}), \quad (24)$$

by conditional LSB sampling. This is compared to the analytical expression of $\langle h_j \rangle_{\mathbf{r}, \beta_{\text{eff}}}$ [Eq. (10)] to estimate β_{eff} (see Sec. II A 2).

In image restoration, conditional generation, and classification, \mathbf{v}_f are set to the intact image pixels, the target class label \mathbf{C} , and the image \mathbf{I} of the test data, respectively.

D. Details of Experiments

In this subsection, we describe the experimental settings.

1. Summary of Parameter Settings

TABLE I. Summary of parameters for each experiment.

Data set	N_v	N_h	N	D	D_{Test}	$L = L'$	M	η
3-spin model	10	5	15	9600	N/A	9600	100	0.05
BAS	42	21	63	96	96	96	250	0.001
OptDigits	64+10	37	111	3823	1797	320	500	0.001

Most parameter values used in the experiments in Sec. II B are summarized in Table I. Common settings and additional details of sampling parameters are described below.

All training was performed with momentum $\alpha = 0.5$ and L_2 regularization $\lambda = 10^{-5}$ applied to V_{ij} and W_{ij} . The initial values of nonzero J_{ij} were sampled from $\mathcal{N}(0, 10^{-4})$ and the initial values of f_i were set to zero.

For LSB sampling, the hyperparameter Δ was fixed to 1 and σ was selected by empirically testing several candidate values and choosing the one that gave good learning performance. For the 3-spin model, σ was optimized for each instance across the candidate set $\sigma^{-2} \in \{0.5, 0.6, \dots, 1.9, 2.0\}$.

For the BAS and OptDigits datasets, σ was set as $\sigma^{-2} = 1.0$ for the BAS and $\sigma^{-2} = 3.5$ for the OptDigits. The selected values were kept fixed during each training. For comparison, CD-100 was also used for the 3-spin model with $\beta = 1$ to train RBMs.

In CEM, the condition vector \mathbf{r} was set to a data vector $\mathbf{v}^{(d)}$ randomly selected from the training dataset.

For OptDigits only, mini-batch learning was employed with a batch size of 382, resulting in ten mini-batches per epoch. Before splitting, the entire training dataset was randomly shuffled to ensure that each mini-batch contained approximately equal proportions of samples from each class.

2. Dataset Preparation

3-spin model: Data were generated according to the exact Boltzmann distribution:

$$B_{3\text{spin}}(\mathbf{v}) = \frac{e^{-E_{3\text{spin}}(\mathbf{v})}}{\sum_{\mathbf{v}} e^{-E_{3\text{spin}}(\mathbf{v})}}, \quad (25)$$

$$E_{3\text{spin}}(\mathbf{v}) = - \sum_{i=1}^{N_v} \sum_{j>i}^{N_v} \sum_{k>j}^{N_v} T_{ijk} v_i v_j v_k, \quad (26)$$

$$T_{ijk} \sim \mathcal{N}\left(0, \frac{\sqrt{3}\zeta}{N_v}\right) \text{ for } 1 \leq i < j < k \leq N_v, \quad (27)$$

where $E_{3\text{spin}}(\mathbf{v})$ denotes the global energy function of the 3-spin model [51, 52], and T_{ijk} represents the three-body interaction coefficients drawn from a Gaussian distribution $\mathcal{N}\left(0, \frac{\sqrt{3}\zeta}{N_v}\right)$ with mean 0 and standard deviation $\sqrt{3}\zeta/N_v$. Ten independent instances were generated, each characterized by a distinct set of T_{ijk} values. Each dataset consisted

of $D = 9600$ samples with $N_v = 10$, obtained via exact Boltzmann sampling by enumerating all visible configurations \mathbf{v} and drawing samples based on exhaustively computed Boltzmann weights $B_{3\text{spin}}(\mathbf{v})$. We set ζ to a sufficiently large value of 2, which is enough to yield a nontrivial spin-glass phase in the thermodynamic limit [51, 52]. The overlap distribution of the generated samples was verified to exhibit spin-glass-like features (see Supplementary Information).

BAS: The bars-and-stripes (BAS) dataset consists of binary images generated by assigning each row or column to either black (-1) or white ($+1$) at random [3, 53]. We constructed a BAS dataset of 7×6 binary images, containing 192 mutually distinct patterns (all possible patterns), each with $N_v = 42$ binary variables. The images were randomly shuffled and split into training and test sets of equal size ($D = D_{\text{Test}} = 96$).

OptDigits: The Optical Recognition of Handwritten Digits (OptDigits) dataset was obtained from the UCI Machine Learning Repository [54]. Each original sample consists of a four-bit grayscale image of 8×8 pixels and a categorical label indicating one of ten digit classes (0–9). For our experiments, each image was flattened into a 64-dimensional image vector \mathbf{I} , and the class label was converted to a 10-dimensional one-hot encoded vector \mathbf{C} . Specifically, for a sample belonging to class $j \in \{0, \dots, 9\}$, the j -th component of \mathbf{C} was set to $+1$, while all other components were set to -1 . Pixel values were binarized by thresholding at the midpoint of the original four-bit gray scale range, mapping them to $\{-1, +1\}$, thus each image vector \mathbf{I} was converted into a 64-dimensional Ising vector. We employed combined representation $\mathbf{v} = (\mathbf{I}^T, \mathbf{C}^T)^T$ as data vector with $N_v = 74$ variable. The final dataset contained $D = 3823$ training samples and $D_{\text{Test}} = 1797$ test samples, with approximately equal proportions across classes.

REFERENCES

-
- [1] Hinton, G. E. & Sejnowski, T. J. Optimal perceptual inference. In *Proceedings of the IEEE conference on Computer Vision and Pattern Recognition*. **448**, 448–453 (1983).
 - [2] Ackley, D. H., Hinton, G. E. & Sejnowski, T. J. A learning algorithm for Boltzmann machines. *Cogn. Sci.* **9**, 147–169 (1985).
 - [3] G. E. Hinton & T. J. Sejnowski. Learning and relearning in Boltzmann machines. *Parallel Distributed Processing: Explorations in the Microstructure of Cognition* Volume 1, Foundations (Cambridge University Press, New York, 1986).
 - [4] Le Roux, N. & Bengio, Y. Representational power of restricted Boltzmann machines and deep belief networks. *Neural Comput.* **20**, 1631–1649. <https://doi.org/10.1162/neco.2008.04-07-510> (2008).
 - [5] Montufar, G., & Ay, N. Refinements of universal approximation results for deep belief networks and restricted Boltzmann machines. *Neural Comput.* **23**, 1306–1319 (2011).
 - [6] Fiore, U., Palmieri, F., Castiglione, A., & De Santis, A. Network anomaly detection with the restricted Boltzmann machine. *Neurocomputing*, **122**, 13–23 (2013).
 - [7] Mnih, A. & Hinton, G. E. Three new graphical models for statistical language modelling. *Proceedings of the 24th international conference on Machine learning*. 641–648 (Association for Computing Machinery, 2007).
 - [8] Hinton, G. E., & Salakhutdinov, R. R. Replicated softmax: an undirected topic model. *Advances in neural information processing systems*, 22, (2009).
 - [9] Huang, L., & Wang, L. Accelerated Monte Carlo simulations with restricted Boltzmann machines. *Phys. Rev. B*, **95**, 035105 (2007).
 - [10] Morningstar, A., & Melko, R. G. Deep learning the ising model near criticality. *J. Mac. Learn. Res.*, **18**, 5975–5991 (2018).
 - [11] Torlai, G. & Melko, R. Learning thermodynamics with Boltzmann machines. *Phys. Rev. B* **94**, 165134 (2016).
 - [12] Carleo, G. & Troyer, M. Solving the quantum many-body problem with artificial neural networks. *Science* **355**, 602–606 (2017).
 - [13] Torlai, G. et al. Integrating neural networks with a quantum simulator for state reconstruction. *Phys. Rev. Lett.* **123**, 230504 (2019).
 - [14] Bengio, Y., Lamblin, P., Popovici, D. & Larochelle, H. Greedy

- layer-wise training of deep networks. *Advances in neural information processing systems* **19**, 153 (2007).
- [15] Hinton, G. E., Osindero, S. & Teh, Y.-W. A Fast Learning Algorithm for Deep Belief Nets. *Neural Comput.* **18**, 1527–1554 (2006).
 - [16] Salakhutdinov, R., & Hinton, G. Deep boltzmann machines. In *Artificial Intelligence and Statistics*, PMLR 448–455 (2009).
 - [17] Hinton, G. & Salakhutdinov, R. An efficient learning procedure for deep Boltzmann machines. *Neural Comput.* **24**, 1967–2006 (2012).
 - [18] LeCun, Y., Bengio, Y., & Hinton, G. Deep learning. *Nature*, **521**, 436–444 (2015).
 - [19] Andrieu, C., De Freitas, N., Doucet, A., & Jordan, M. I. An introduction to MCMC for machine learning. *Machine learning*, **50**, 5–43 (2003).
 - [20] Geman, S., & Geman, D. Stochastic relaxation, Gibbs distributions, and the Bayesian restoration of images. *IEEE Trans. Pattern Anal. Mach. Intell.* **6**, 721–741 (1984).
 - [21] Hastings, W. K. Monte Carlo sampling methods using Markov chains and their applications. *Biometrika* **57**, 97–109 (1970).
 - [22] Metropolis, N., Rosenbluth, A. W., Rosenbluth, M. N., Teller, A. H., & Teller, E. Equation of state calculations by fast computing machines. *J. Chem. Phys.* **21**, 1087–1092 (1953).
 - [23] Smolensky, P. Information processing in dynamical systems: foundations of harmony theory. In *Parallel Distributed Processing: Explorations in the Microstructure of Cognition* (eds Rumelhart, D. E., McClelland, J. L. & CORPORATE PDP Research Group) 194–281 (MIT Press, Cambridge, 1986).
 - [24] Freund, Y. & Haussler, D. *Unsupervised Learning of Distributions of Binary Vectors Using Two Layer Networks*. Report No. UCSC-CRL-91-20 (University of California, 1994).
 - [25] Fischer, A. & Igel, C. Training restricted Boltzmann machines: an introduction. *Pattern Recogn.* **25**, 25–39 (2014).
 - [26] Hinton, G. A practical guide to training restricted boltzmann machines. In *Neural Networks: Tricks of the Trade, Vol. 7700 of Lecture Notes in Computer Science* (eds Montavon, G., Orr, G. B. & Müller, K.-R.) 599–619 (Springer, Berlin Heidelberg, 2012).
 - [27] Osindero, S. & Hinton, G. E. Modeling image patches with a directed hierarchy of Markov random fields. *Advances in Neural Information Processing Systems* **20**, (eds J.C. Platt, D. Koller, Y. Singer & S. Roweis) (MIT Press, Cambridge, 2008).
 - [28] Salakhutdinov, R. Learning and evaluating Boltzmann machines. Technical Report UTML TR 2008-002, Department of Computer Science, University of Toronto 2008.
 - [29] Schulz, H., Müller, A. & Behnke, S. Exploiting local structure in stacked Boltzmann machines. In *European Symposium on Artificial Neural Networks, Computational Intelligence and Machine Learning (ESANN)*, 2010.
 - [30] Goto, H., Tatsumura, K. & Dixon, A. R. Combinatorial optimization by simulating adiabatic bifurcations in nonlinear Hamiltonian systems. *Sci. Adv.* **5**, eaav2372. (2019).
 - [31] Goto, H. et al. High-performance combinatorial optimization based on classical mechanics. *Sci. Adv.* **7**, eabe7953 (2021).
 - [32] Kanao, T. & Goto, H. Simulated bifurcation assisted by thermal fluctuation. *Commun. Phys.* **5**, 153 (2022).
 - [33] Kanao, T. & Goto, H. Simulated bifurcation for higher-order cost functions. *Appl. Phys. Express* **16**, 014501 (2023).
 - [34] Goto, H., Hidaka, R., & Tatsumura, K. Harnessing the edge of chaos for combinatorial optimization. *arXiv preprint arXiv:2508.17655* (2025).
 - [35] Johnson, M. W. et al. Quantum annealing with manufactured spins. *Nature* **473**, 194–198 (2011).
 - [36] Harris, R. et al. Experimental investigation of an eight-qubit unit cell in a superconducting optimization processor. *Phys. Rev. B* **82**, 024511. (2010).
 - [37] Bunyk, P. I. et al. Architectural considerations in the design of a superconducting quantum annealing processor. *IEEE Trans. Appl. Supercond.* **24**, 1–10 (2014).
 - [38] Boothby, K., Bunyk, P., Raymond, J., & Roy, A. Next-generation topology of d-wave quantum processors. *arXiv preprint arXiv:2003.00133* (2020).
 - [39] Amin, M. H. Searching for quantum speedup in quasistatic quantum annealers. *Phys. Rev. A* **92**, 052323 (2015).
 - [40] Adachi, S. H. & Henderson, M. P. Application of quantum annealing to training of deep neural networks. *arXiv preprint arXiv: 1510.06356* (2015).
 - [41] Dixit, V. et al. Training a quantum annealing based restricted Boltzmann machine on cybersecurity data. *IEEE Trans. Emerg. Top. Comput. Intell.* **6**, 417–428 (2021).
 - [42] Sato, T., Ohzeki, M. & Tanaka, K. Assessment of image generation by quantum annealer. *Sci. Rep.* **11**, 13523. (2021).
 - [43] Inagaki, T. et al. A coherent Ising machine for 2000-node optimization problems. *Science* **354**, 603–606 (2016).
 - [44] McMahon, P. L. et al. A fully programmable 100-spin coherent Ising machine with all-to-all connections. *Science* **354**(6312), 614–617 (2016).
 - [45] Hiroki, T. et al. Observing a phase transition in a coherent Ising machine. *Phys. Rev. Appl.* **19**, L031001 (2023).
 - [46] Tiunov, E. S., Ulanov, A. E. & Lvovsky, A. I. Annealing by simulating the coherent Ising machine. *Opt. Express* **27**, 10288 (2019).
 - [47] Ulanov, A. E., Tiunov, E. S. & Lvovsky, A. I. Quantum-inspired annealers as Boltzmann generators for machine learning and statistical physics. *arXiv preprint arxiv: 1912.08480* (2019).
 - [48] Raymond, J., Yarkoni, S. & Andriyash, E. Global warming: Temperature estimation in annealers. *Front. ICT* **3**, 23. (2016).
 - [49] Benedetti, M., Realpe-Gómez, J., Biswas, R. & Perdomo-Ortiz, A. Estimation of effective temperatures in quantum annealers for sampling applications: A case study with possible applications in deep learning. *Phys. Rev. A* **94**, 022308 (2016).
 - [50] Benedetti, M., Realpe-Gómez, J., Biswas, R. & Perdomo-Ortiz, A. Quantum-Assisted Learning of Hardware-Embedded Probabilistic Graphical Models, *Phys. Rev. X*, **7**, 041052 (2017).
 - [51] Mézard, M., Parisi, G. & Virasoro, M. A. *Spin Glass Theory and Beyond* (World Scientific, 1987).
 - [52] Mézard, M. & Montanari, A. *Information, Physics, and Computation* (Oxford University Press, 2009).
 - [53] MacKay, D. J. C. *Information Theory, Inference and Learning Algorithms* (Cambridge Univ. Press, Cambridge, 2003).
 - [54] Lichman, M. *UCI machine learning repository*, <http://archive.ics.uci.edu/ml/> (2013).
 - [55] Rossky, P. J., Doll, J. D. & Friedman, H. L. Brownian dynamics as smart Monte Carlosimulation. *J. Chem. Phys.* **69**, 4628–4633 (1978).
 - [56] Roberts, G. O. & Stramer, O. Langevin diffusions and Metropolis-Hastings algorithms. *Methodol. Comput. Appl. Probab.*, **4**, 337–357 (2002).
 - [57] Leimkuhler, B. & Reich, S. *Simulating Hamiltonian Dynamics* (Cambridge Univ. Press, Cambridge, 2004).
 - [58] Virtanen, P. et al. SciPy 1.0: fundamental algorithms for scientific computing in Python. *Nat. Methods* **17**, 261–272 (2020)

SUPPLEMENTARY INFORMATION

Appendix A: Comparison with Other β_{eff} estimation methods

In Fig. 9, we compare β_{eff} estimated by various methods for LSB output distribution shown in Sec. II A 1 in the main text. The results of CEM and KL-divergence minimization are identical to those in Fig. 2(b) in the main text.

In CEM- n approach, we consider n distinct conditions $\{\mathbf{r}^{(m)} | m = 1, \dots, n\}$ and estimate β_{eff} using the modified expression: $\beta_{\text{eff}} = \text{argmin}_{\beta > 0} \sum_{m=1}^n F_{\mathbf{r}^{(m)}}(\beta)$. CEM introduced in the main text is identical to CEM-1. For CEM-3 and 5, each component of the condition vectors $\{\mathbf{r}^{(m)} | m = 1, \dots, n\}$ was uniformly sampled in $\{-1, 1\}$. The mean signed relative error between them across 10 instances is approximately $3.6 \pm 1.3\%$, $3.9 \pm 1.3\%$, and $3.8 \pm 1.3\%$ for CEM- n with $n = 1, 3$, and 5, respectively. These results indicate that CEM- n ($n \in \{1, 3, 5\}$) exhibit comparable performance within the standard error. Furthermore, the estimation error of β_{eff} using CEM- n tends to shift toward lower temperatures.

The MLPL in Fig. 9 refers to maximum log-pseudo-likelihood estimation [48, 49], a method commonly regarded as efficient, though its accuracy has been questioned. In the results, we found that its signed relative error to KL was $-4.0 \pm 1.1\%$, which was comparable in absolute magnitude to that of CEM. However, MLPL exhibited a bias toward higher estimated temperatures, in contrast to CEM. Furthermore, when MLPL was used instead of CEM for inverse temperature estimation in SAL, the learning performance of SRBMs deteriorated significantly (see Sec. C). This deterioration can be attributed to the opposing bias tendencies in the inverse temperature estimates produced by MLPL and CEM.

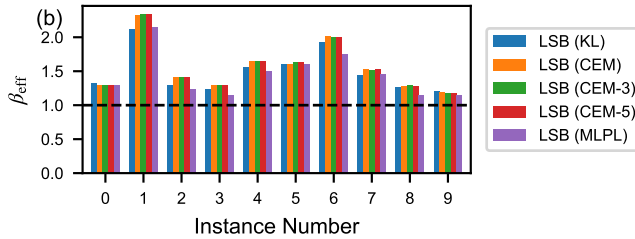


FIG. 9. **Effective inverse temperature for LSB:** The effective inverse temperature β_{eff} for the output distribution produced by LSB. Inverse temperature β_{eff} was estimated by KL-divergence minimization, CEM- n with $n = 1, 3, 5$ where $\{\mathbf{r}^{(m)} | m = 1, \dots, n\}$ were randomly generated Ising vectors, and MLPL.

Appendix B: Sampling Performance on SK Model

In this section, we study the sampling performance on the Sherrington–Kirkpatrick (SK) model:

$$E_{\text{SK}}(\mathbf{s}) = - \sum_{i=1}^N \sum_{j>i}^{N_v} J_{ij} s_i s_j, \quad (\text{B1})$$

$$J_{ij} \sim \mathcal{N}\left(0, \frac{\zeta}{\sqrt{N}}\right) \quad \text{for } 1 \leq i < j \leq N, \quad (\text{B2})$$

where $E_{\text{SK}}(\mathbf{s})$ denotes the global energy function of the SK model (the 2-spin model) [51, 52], and J_{ij} represents the pairwise interaction coefficients drawn from a Gaussian distribution $\mathcal{N}\left(0, \frac{\zeta}{\sqrt{N}}\right)$ with mean 0 and standard deviation ζ/\sqrt{N} . The SK model is a fully connected spin-glass system, making the sampling task substantially more complex than the SRBM case discussed in Sec. II A 1 of the main text. We executed sampling tasks for ten random instances, each characterized by a distinct set of J_{ij} values. The parameter ζ was set to a sufficiently large value of 2 to yield a nontrivial spin-glass phase at $\beta = 1$ [51, 52]. We sampled $D = 9600$ Ising vectors \mathbf{s} with $N = 15$ using various sampling methods.

Figure 10(a) indicates that the sampling accuracy of LSB and that of Gibbs sampling with $\beta = 1$ are comparable within the standard error, similarly to the results discussed for SRBMs in the main text. Here, cLSB refers to a variant of LSB in which the discretization procedure [Eq. (8)] is replaced by a clipping rule of bSB and dSB [31]:

$$x_i \rightarrow \begin{cases} 1 & \text{for } x_i \geq 1, \\ x_i & \text{for } -1 < x_i < 1, \\ -1 & \text{for } x_i \leq -1. \end{cases} \quad (\text{B3})$$

Despite the relatively high sampling accuracy of cLSB, LSB achieves better sampling performance for all instances.

Figure 10(b) shows the inverse temperature, obtained via KL-divergence minimization, corresponding to sampling results of panel (a). It was confirmed that the inverse temperature of the output distributions from LSB and cLSB also depends on the instance, similarly to what was observed in main text.

Figure 10(c) shows the sampling accuracy of conventional SB algorithms: aSB, bSB, and dSB. Although we tuned the parameters to achieve the best possible accuracy (see the caption of Fig. 10 for details of parameters), the sampling accuracy of these conventional SBs are clearly inferior to that of Gibbs sampling, LSB, and cLSB. Among them, bSB exhibits the poorest performance [highest $D_{\text{KL}}(P_S || B_{\beta_{\text{eff}}})$]. Although not shown in the figure, we have found that using variants such as HbSB and HdSB [32], which are modified versions of bSB and dSB, can improve the sampling accuracy. However, even with these improvements, the performance has not surpassed that of LSB and cLSB. These results indicate that our proposed enhancement method, (c)LSB, is indeed meaningful.

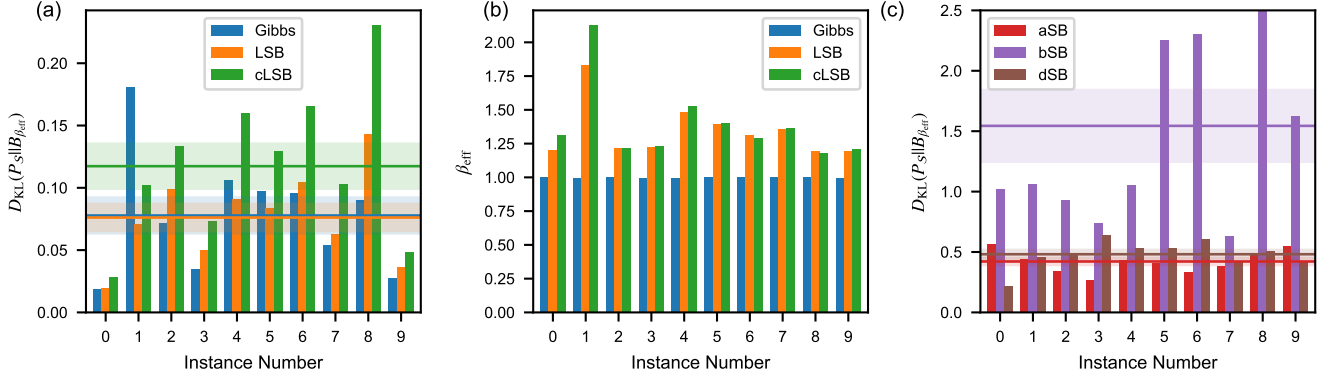


FIG. 10. **Sampling accuracy $D_{\text{KL}}(P_S||B_{\beta_{\text{eff}}})$ and effective temperature β_{eff} across ten SK model instances for various sampling methods:** The horizontal axis of all panels indicates the instance number. Panel (a) shows $D_{\text{KL}}(P_S||B_{\beta_{\text{eff}}})$ for LSB, Gibbs, and cLSB. Panel (b) shows β_{eff} estimated by KL-divergence minimization corresponding to panel (a). Panel (c) shows $D_{\text{KL}}(P_S||B_{\beta_{\text{eff}}})$ for aSB, bSB, and dSB. In panel (a) and (c), horizontal lines and shaded regions indicate the means $D_{\text{KL}}(P_S||B_{\beta_{\text{eff}}})$ and their standard errors. Parameter settings in these sampling experiments were as follows: The number of iteration steps for SB-related methods and the number of Monte Carlo steps for Gibbs sampling were both set to $M = 100$. For LSB and cLSB, the discretization step size Δ was set to 1, and σ was optimized from the candidate set $\sigma^{-2} \in \{0.5, 0.6, \dots, 1.9, 2.0\}$ to maximize sampling accuracy. For aSB, bSB, and dSB, parameters were set according to the notation in Ref. [31]: $dt = 1.0$, $a_0 = 1.0$, $a(t) = 0$ for all methods, and c_0 was set to 1.0 for aSB, $\sqrt{\sum_{j=1}^N x_j^2 / [\sum_{i=1}^N (\sum_{j=1}^N J_{ij} x_j)^2]}$ for bSB, and $\sqrt{N / \{\sum_{i=1}^N [\sum_{j=1}^N J_{ij} \text{sgn}(x_j)]^2\}}$ for dSB.

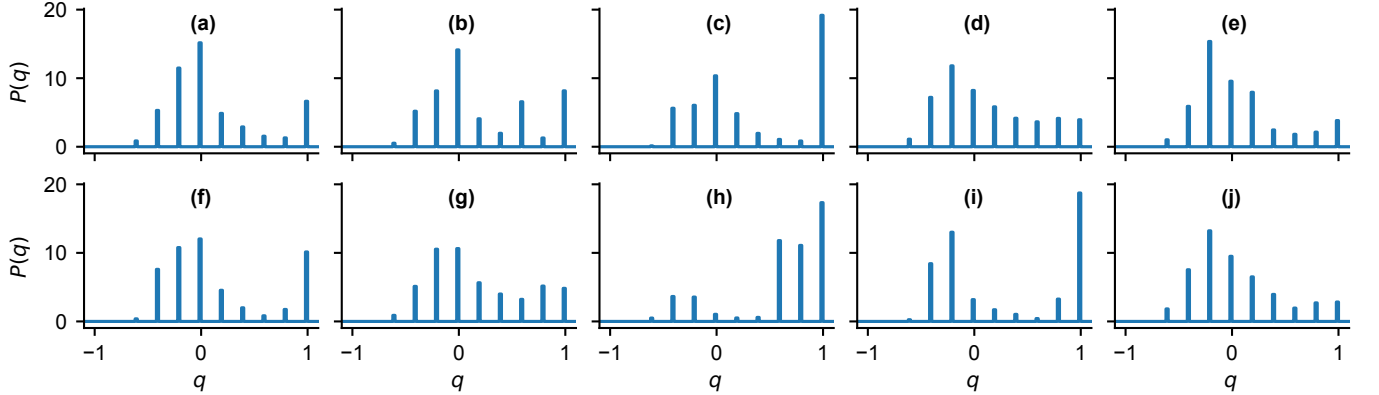


FIG. 11. **Overlap distributions for all instances:** Each panel shows the overlap distribution $P(q)$ for one of the 10 dataset instances. All instances exhibit nontrivial spin-glass features.

Appendix C: Additional Information on the 3-spin model

1. Overlap Distribution

We analyze the overlap distribution of the 3-spin model dataset discussed in the main text. For a given instance $\{\mathbf{v}^{(d)} | d = 1, \dots, D\}$, we consider the overlap between $\mathbf{v}^{(\mu)}$ and $\mathbf{v}^{(\rho)}$:

$$q^{(\mu, \rho)} = \frac{1}{N_v} \sum_{i=1}^{N_v} v_i^{(\mu)} v_i^{(\rho)}, \quad (\text{C1})$$

and construct the corresponding histogram across all samples $P(q)$ [51, 52]. All instances exhibit nontrivial overlap distributions that are neither paramagnetic, characterized by a single

peak centered at $q = 0$, nor ferromagnetic or antiferromagnetic, both characterized by two peaks located near $q = \pm 1$, as shown in Fig. 11. These observations indicate that the dataset reflects a genuine spin-glass regime and possesses nontrivial structures.

2. Sampling Accuracy and β_{eff} During Training

This subsection tracks the evolution of sampling accuracy, measured by $D_{\text{KL}}(P_S||B_{\beta_{\text{eff}}})$, and the effective inverse temperature β_{eff} throughout the learning process described in the main text (Sec. II B 1).

Figure 12 shows the evolution of sampling accuracy, measured by $D_{\text{KL}}(P_S||B_{\beta_{\text{eff}}})$, during training on the 3-spin model

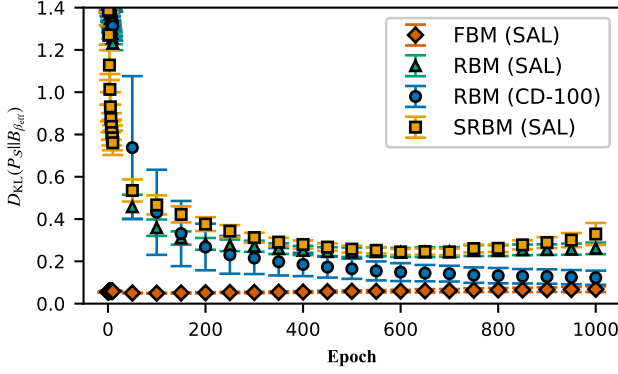


FIG. 12. **Evolution of sampling accuracy $D_{\text{KL}}(P_S || B_{\beta_{\text{eff}}})$ during training on the 3-spin model:** The horizontal axis shows the training epoch, and the vertical axis shows the KL divergence between the sampled distribution P_S and the Boltzmann distribution $B_{\beta_{\text{eff}}}$ at the estimated effective inverse temperature β_{eff} .

discussed in the main text (Sec. II B 1). LSB in FBMs achieved the smallest $D_{\text{KL}}(P_S || B_{\beta_{\text{eff}}})$, which is reasonable because FBMs use $N = 10$ visible units, whereas RBMs and SRBMs use $N = 15$, making sampling inherently more challenging for the latter. Nevertheless, it is noteworthy that the sampling accuracy achieved by LSB in FBMs surpassed that of CD-100 in RBMs. The sampling accuracy of LSB in SRBMs and RBMs was comparable to CD-100 in RBMs during the early stages. Although the former became slightly inferior after about 350 epochs, the overall training performance remained comparable to or even surpassed that of the latter, as detailed in the main text. These results highlight the effectiveness of LSB as parallel Boltzmann samplers for BM training.

Figure 13 illustrates how the effective inverse temperature β_{eff} of SAL-trained SRBMs evolves throughout the training process for the 3-spin model (see Sec. II B 1 in the main text). For each instance (panels a–j), the trajectories of β_{eff} estimated by KL-based method and CEM are compared across training epochs. Although there are a few exceptional instances, such as (a), the CEM estimators generally

provide stable and reliable estimates of β_{eff} throughout training, closely matching the KL-based estimator. Although not shown, a similar trend was observed for RBMs as well. These results underscore the robustness of CEM for inverse temperature estimation in practical Boltzmann machine learning.

3. Comparison with other learning methods

Figure 14 shows the learning performance of SRBMs trained with SAL to RBMs and SRBMs trained using alternative methods not discussed in the main text.

First, the performance of RBMs trained with CD-1 was markedly inferior to that of Blocked Gibbs (BG) sampling with 100 iterations, which yields performance nearly equivalent to CD-100 in the main text. In contrast, CD-10 achieved performance comparable to BG, highlighting the rapid convergence of the CD method. However, even when RBMs were successfully trained using CD-10 or BG their performance did not reach that of SRBMs trained with SAL.

Replacing CEM in SAL with the MLPL (maximum log-pseudo-likelihood) β_{eff} estimator [48, 49] resulted in SRBM performance nearly identical to that of RBMs trained with CD-10 or BG. This performance degradation may be attributed to the opposing bias tendencies of CEM and MLPL (see Sec. A).

Because visible variables are not independent, CD is theoretically inappropriate in SRBMs. In our experiments, CD-1 for learning SRBMs led to severe degradation, with $D_{\text{KL}}(P_D || Q_\beta)$ increasing substantially as learning progressed. Although not shown in the figure, SRBMs trained with CD-10 and CD-100 exhibited even poorer and highly unstable performance. Previous reports have suggested that CD combined with damped mean-field iterations (DMFI) for visible variables could be effective for SRBMs [27, 29]. However, this method also achieved even lower performance than RBMs trained with CD-1, highlighting the limitations of CD-based methods for SRBMs.

These findings suggest that SAL stands out as a highly effective approach for enabling SRBMs to fully exploit their enhanced representational capacity, achieving performance levels unattainable by conventional training methods.

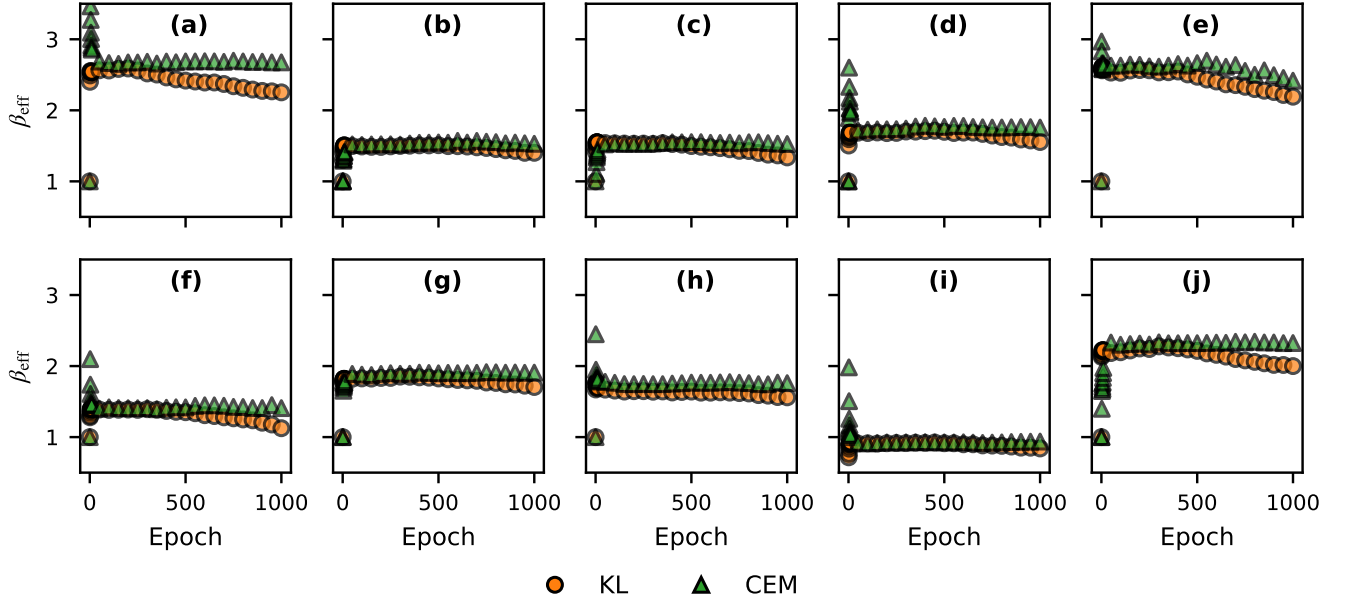


FIG. 13. **Evolution of the effective inverse temperature β_{eff} during training on the 3-spin model:** Each panel (a)–(j) shows the trajectory of β_{eff} estimated by the KL-based method and CEM for individual instances. The horizontal axis represents the training epoch, and the vertical axis indicates the estimated value of β_{eff} .

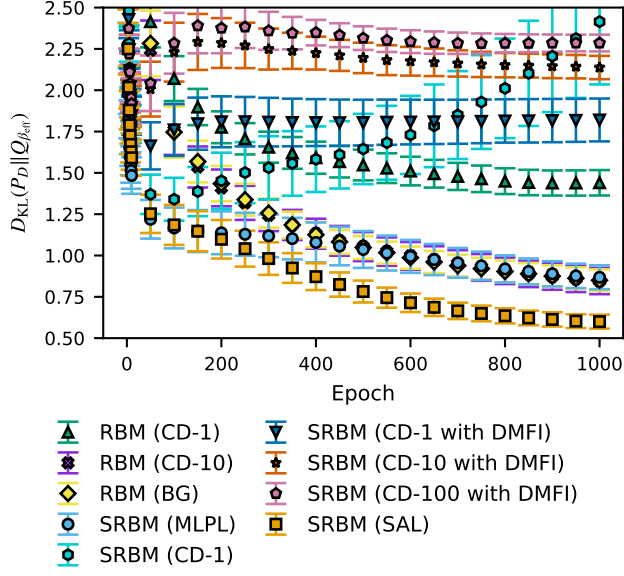


FIG. 14. Further comparison of learning performance on the 3-spin model: The vertical axis shows the cost function $D_{\text{KL}}(P_D || Q_\beta)$, and the horizontal axis indicates training epochs. Nine models are compared: RBMs trained using CD-1, CD-10, and Blocked Gibbs (BG) sampling with 100 Monte Carlo steps; SRBMs trained using SAL in which CEM was replaced with MLPL [48, 49]; SRBMs trained using CD-1; SRBMs trained using CD-1, CD-10, and CD-100 with damped mean-field iterations (DMFI) [27]; and SRBMs trained using SAL. In the DMFI procedure, we used 5 iterations with a damping factor of 0.5. The number of hidden variables N_h for both RBMs and SRBMs was set to 5 as in the main text. Each point represents the mean over the same 10 independent instances used for training in the main text, and error bars denote the standard error.